PROCEEDINGS OF SPIE

SPIEDigitalLibrary.org/conference-proceedings-of-spie

A novel framework for the temporal analysis of bone mineral density in metastatic lesions using CT images of the femur

Tom H. Knoop, Loes C. Derikx, Nico Verdonschot, Cornelis H. Slump

Tom H. Knoop, Loes C. Derikx, Nico Verdonschot, Cornelis H. Slump, "A novel framework for the temporal analysis of bone mineral density in metastatic lesions using CT images of the femur," Proc. SPIE 9414, Medical Imaging 2015: Computer-Aided Diagnosis, 94143A (20 March 2015); doi: 10.1117/12.2081916

SPIE.

Event: SPIE Medical Imaging, 2015, Orlando, Florida, United States

A novel framework for the temporal analysis of bone mineral density in metastatic lesions using CT images of the femur

Tom H. Knoop[a], Loes C. Derikx[b,c], Nico Verdonschot[b,d] and Cornelis H. Slump[a]

[a]MIRA Institute for Biomedical Engineering and Technical Medicine, University of Twente, Enschede, Netherlands

[b]Orthopaedic Research Laboratory, Radboud university medical center, Nijmegen, The Netherlands

[c]Human Movement Biomechanics Research Group, KU Leuven, Leuven, Belgium

[d]Laboratory of Biomechanical Engineering, University of Twente, Enschede, The Netherlands

ABSTRACT

In the progressive stages of cancer, metastatic lesions in often develop in the femur. The accompanying pain and risk of fracture dramatically affect the quality of life of the patient. Radiotherapy is often administered as palliative treatment to relieve pain and restore the bone around the lesion. It is thought to affect the bone mineralization of the treated region, but the quantitative relation between radiation dose and femur remineralization remains unclear. A new framework for the longitudinal analysis of CT-scans of patients receiving radiotherapy is presented to investigate this relationship.

The implemented framework is capable of automatic calibration of Hounsfield Units to calcium equivalent values and the estimation of a prediction interval per scan. Other features of the framework are temporal registration of femurs using `elastix`, transformation of arbitrary Regions Of Interests (ROI), and extraction of metrics for analysis. Build in `Matlab`, the modular approach aides easy adaptation to the pertinent questions in the explorative phase of the research.

For validation purposes, an in-vitro model consisting of a human cadaver femur with a milled hole in the intertrochanteric region was used, representing a femur with a metastatic lesion. The hole was incrementally stacked with plates of PMMA bone cement with variable radiopaqueness. Using a Kolmogorov-Smirnov (KS) test, changes in density distribution due to an increase of the calcium concentration could be discriminated. In a 21 cm^3 ROI, changes in 8% of the volume from 888 $\pm 57 mg \cdot ml^{-1}$ to 1000 $\pm 80 mg \cdot ml^{-1}$ could be statistically proven using the proposed framework. In conclusion, the newly developed framework proved to be a useful and flexible tool for the analysis of longitudinal CT data.

Keywords: Registration, Calibration, Bone mineral density, CT, Elastix, Temporal analysis, Metastatic lesion, Femur

1. INTRODUCTION

Metastatic lesions in the femur often occur in cancer patients in the progressive stages of their disease. The lesions provide multiple problems, such as pain and increased risk of fracture.[1] Currently, an often used palliative treatment for painful metastatic lesions in the femur is radiotherapy, which can be administered in either single- or multiple fraction. The relationship between the two types of radiotherapy on different qualitative descriptors as pain response,[2] analgistic response[3] and quality of life[4] have been studied, amongst others in the Dutch Bone Metastasis Study.[5] However, the relationship between the type of radiotherapy and quantitative effects such as the remineralization rate can still be further investigated.[6] There are indications that the effects of radiotherapy on mineralization are small.[7]

Further author information: (Send correspondence to C.H.S.)
Cornelis H. Slump: E-mail: c.h.slump@utwente.nl

Medical Imaging 2015: Computer-Aided Diagnosis, edited by Lubomir M. Hadjiiski, Georgia D. Tourassi,
Proc. of SPIE Vol. 9414, 94143A · © 2015 SPIE · CCC code: 1605-7422/15/$18 · doi: 10.1117/12.2081916

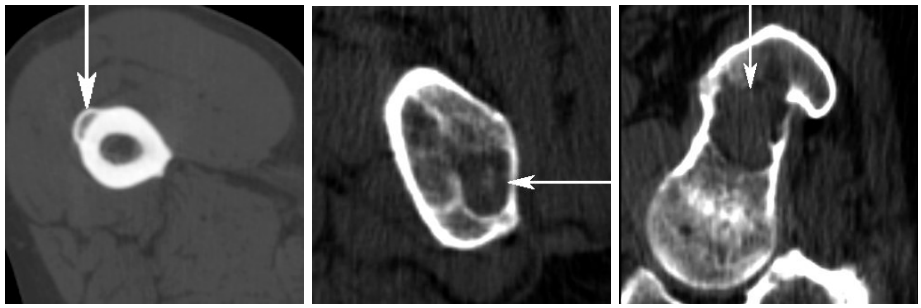

(a) (b) (c)

Figure 1. Example of different appearances of metastatic lesions in the images in the test set. The lesions are both inside and outside the bone, and have various appearances in shape, size and anatomical organization.

The remineralization rate is an important objective parameter for the succes of radiotherapy. It can be seen as the speed at which the osteoblasts repair tissue damaged due to the radiotherapy, by replacing it with newly formed calcium phosphate. It is thought that the body overcompensates for the damage done by the radiation. This should result in changes in the mineralization. The properties of bone will be covered in appendix A.

To investigate the relationship between the radiation dose and bone mineralization in metastatic lesions of the femur, CT scans used for the planning of radiotherapy were collected and analysed. A group of patients receiving either single- or multiple fraction radiotherapy were scanned before, during and after the therapy. These planning scans are more suitable for quantitative analysis than traditional projection X-ray. However, the qualitative purposes lead to very coarse scanning parameters of typically $1 \times 1 \times 3$ mm^3 spatial resolution, and standard deviation of around 11 HU at 120kVp. Quantitative analysis with these parameters is a challenge.

In this group of patients, different types of lesions were present. Some examples of these are shown in figure 1. To analyse the scans in an objective and reliable manner independent of clinical experts' assessments, an automated analysis framework is desired. In this paper, the framework implementation and requirements for calibration of Hounsfield units to calcium concentrations, temporal registration of femurs and data acquisition are presented.

2. FRAMEWORK

The proposed volume framework consists of multiple building blocks. The basic blocks will be described below. These are, calibration, registration and volumetric analysis. The blocks are implemented in `Matlab` and can easily be connected to form an analysis system. The modular approach also aides tailoring the blocks for different research questions.

2.1 Calibration

Calibration is used for two related problems. First, the normalization of the intensity scale to the same known intensity distribution enables the measurement of small inter- and intrapatient effects. Second, the conversion of HU to hydroxyapatite concentrations enables the comparison with known physical properties, and thus provide a physical measure for the comparisons between patients. This is of importance, since the mineral density is somewhat related to the bone strength.[8]

In the protocol for the CT-scans a calibration phantom (QCT-Bone mineral Phantom, Image Analysis, Inc., Columbia, KY, USA) was specified. This phantom consists of four rods with hydroxyapatite concentrations of 0, 50, 100 and 200 mg $\cdot$ ml^{-1}, and a plastic with water-like attenuation. The voxels from the calibration rods were automatically extracted by a part of the framework for further processing. A graphic overview of the phantom used is shown in figure 2.

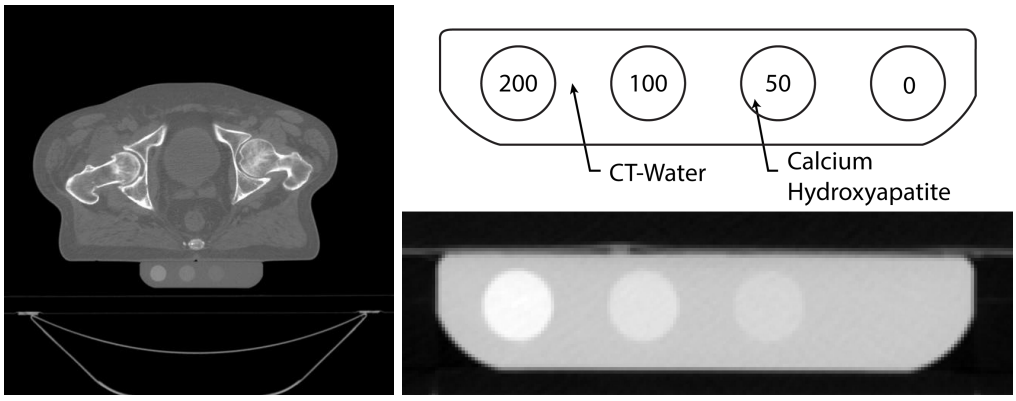

(a) Transversal slice (b) Phantom detail

Figure 2. Cross section of the QCT-Bone Mineral Phantom, used in the patient scans. The (a) image shows a transversal slice with the phantom underneath. The (b) image shows a detail of the phantom (bottom), and a graphical overview of the mineral concentrations (top). The numbers indicate Calcium Hydroxyapatite concentration in mg/ml. Adapted from.[9]

Using weighted least squares regression, a first order function was estimated which maps the obtained HU from the phantom to a certain hydroxyapatite concentration. The prediction interval,[10] mostly due to CT noise in the original image, was also calculated, as well as the confidence interval for the regression. The total calibration function is as follows:

$$\hat{X}_i = \hat{\alpha_0} \pm \mathrm{ci}_{\hat{\alpha}0} + (\hat{\alpha}_1 \pm \mathrm{ci}_{\hat{\alpha}1})\, Y_i \pm \mathrm{PI}. \tag{1}$$

In equation 1, the Hounsfield number Y_i corresponds with an estimated mineral density $\hat{X}_i$. Both regression parameters $\hat{\alpha}_{0,1}$ have a confidence interval ci. The prediction interval PI is derived from the following formula:

$$\mathrm{PI}\,(x) = t_{n-2,\alpha}\hat{\sigma}\left(1 + \frac{1}{n} + \frac{\left(x - \overline{X}\right)^2}{(n-1)\,\sigma_x^2}\right)^{1/2}, \tag{2}$$

where is t t-value for a two tailed student t-test with n measurements. $\hat{\sigma}$ is the mean residual sum of squares from an ANOVA on the linear regression. $\overline{X}$ is the mean value of the measured calibration points, and σ_x^2 is the measured variance in the calibration points. Since n is very large, typically above 90.000, the x dependent terms in equation 2 can be set at a constant value. Therefore, the prediction interval is taken as a constant, only depending on the image variance σ.

2.2 Registration

Registration is used to track anatomical positions in the femur over different scans. This is necessary for any temporal quantitative analysis. In this framework, rigid registration of single femurs was done automatically with `elastix`,[11,12] using a coupling with `Matlab`. Because the interest lies with longitudinal studies on the femur, it can be assumed that the femur of a single patient does not change in size or shape over time. Since the femur is a rigid structure, a rigid (euler) masked registration proved suitable. The mask identifies the voxels belonging to a specific femur, and is made manually for the first scan in a series. It is then propagated to the other scans in that series.

The registration process uses the the mean squared difference (MSD) as cost function to calculate the match between two images with a certain alignment. A lower value implies better spatial alignment. The result is a transformation function $T_{\vec{\mu}}(\vec{x})$, which relates the moving images $\mathrm{I_M}(\vec{x})$ and the fixed image $\mathrm{I_F}(\vec{x})$ in such a way that:

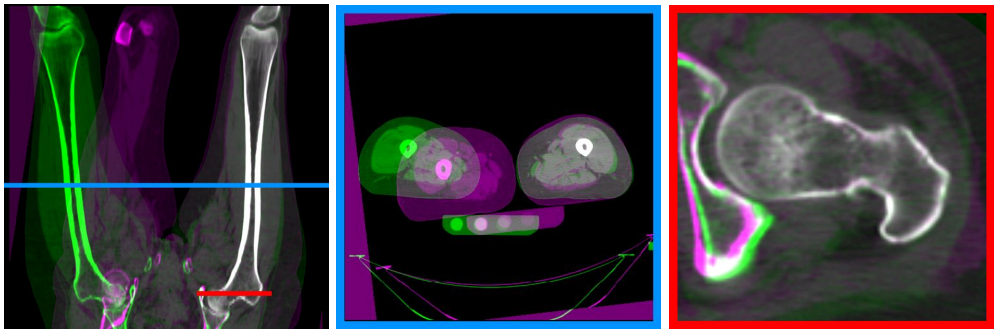

(a) Coronal plane (b) Transversal, large cutout (c) Transversal, small cutout

Figure 3. Overlay images of two CT volumes, registered at the right femur. The lines in the (a) image show the location of the transversal slices at the upper line (b) and the lower line (c).

$$\mathrm{I_F}\left(\vec{x}\right) = \mathrm{I_M}\left(T_{\vec{\mu}}\left(\vec{x}\right)\right). \tag{3}$$

The transformation functions are defined by a set of parameters, $\vec{\mu}$. These are saved by the registration subfunction to be used in later stages. In that way, the time consuming registration process only has to be performed once for multiple studies. It also enables the propagation of arbitrary ROI's throughout a series of scans, to analyze only parts of a femur, e.g. only the area receiving radiotherapy.

As a metric for registration success, the MSD was compared to four times the squared standard deviation found in the calibration process. This is an arbitrary measure for the noise present in the image, and has a loose relationship with the theoretical MSD for perfectly aligned images within the noise boundary. However, the MSD can only indicate a failed registration, as it is based on assumed similarities between two volumes. Therefore, a visual inspection such as shown in figure 3 can be usefull.

2.3 Volumetric analysis

The final goal of the framework is the analysis of the calibrated and registered CT data. Because of the flexible nature of the framework, the output metrics calculation can be tailored to the needs of the researcher using the framework. In its most general form, a metric is calculated for all images in the series, and then compared with other intra or inter patient metrics in a large statistical analysis. The simpelest example of such a metric is the one dimentional mean calibrated intensity for all voxels in the femoral head, which might give an indication of the overall calcification of the bone.

More complicated is the comparison of distributions amongst volumes, which can be done using a two-sample Kolmogorov-Smirnov (KS) test.[13] For this test, the empirical calcium density distribution function $F_n\left(x\right)$ is

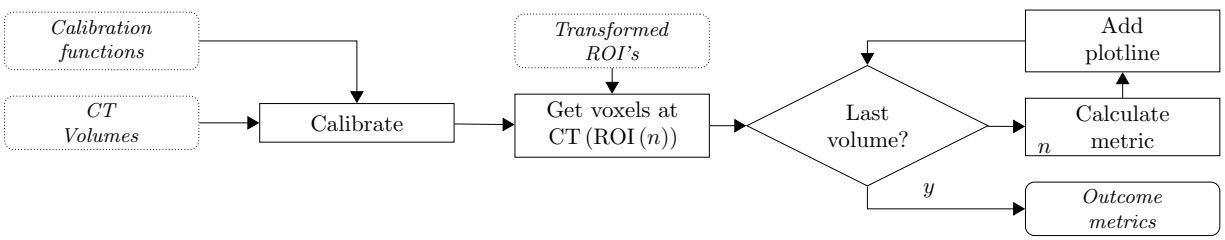

Figure 4. Example of a volume analysis block. CT volumes, calibration functions and Regions of Interest (usually parts of femur segmentations) are inputted, and used to calculate metrics on the same anatomical volumes in different images.

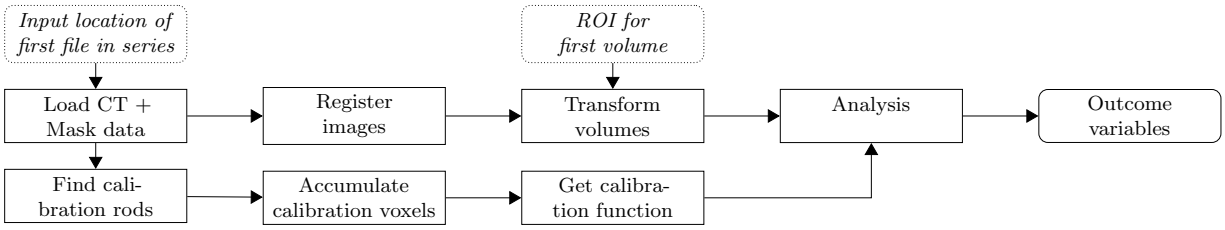

Figure 5. Flowchart of a combination of building blocks for the analysis of volumes.

estimated, and tested for being equal to the calcium density distribution function of another volume. The emperical density distribution function is defined as follows:

$$F_n(x) = \frac{1}{n}\sum_{i=1}^{n} I_X \leq x_i. \tag{4}$$

With I_X the empirical chance of a voxel having a calcium concentration less or equal to the calcium concentration x_i. The outcome of the KS test is a rejection or acceptance of the null hypothesis that two empirical distributions originate from the same continuous distribution.

A typical example of a volume analysis scheme is shown in figure 4. This scheme contains functions extraction of data from the volumes, the calibration of CT data, and the metric calculation and overview plot per image in the series.

2.4 Volume framework

The novel volume framework consists of multiple building blocks, most of which have been described in the previous parts. The blocks can easily be combined in `Matlab` to form an analysis system. For future use, the blocks aid easy adjustment to specific research questions. An example of an analysis system using the blocks is shown in figure 5. The calibration functions are described in the lower row of this figure, as they are parallel to the transformation process. This way, it is possible to change the method of calibration without having to change the accumulation of the calibration data.

If need to, the analysis block can be changed to a data extraction part, so the actual analysis can be performed on larger datasets of multiple patients using a dedicated program. In this work, the mean bone mineral density and the intensity distribution have been chosen as examples of one- and two-dimensional outcome variables.

The input blocks on the top row are typically the source CT data, and a region of interest to extract the data from. With volumetric analysis it is chosen to transform the ROI's, and keep the CT volumes as they are to minimize the interpolation errors in transforming the volumes. However, it is possible to transform the CT as well, to aid voxel-based comparisons.

3. VALIDATION

To assess the performance of the system shown in figure 5, it was analysed using a custom in vitro model. This model consisted of a human cadaver femur with a hole milled in the intertrochantic region , which was filled with radiopaque plates of bone cement (PMMA, Stryker surgical simplex P). The PMMA plates had a CT-measured hydroxyapatite density of 888 $\pm 57\text{mg} \cdot \text{ml}^{-1}$. Another set of plates was made with PMMA with 1% wt Barium Sulphate added, to become approximately 100 HU more radiopaque,[14] a material now called HD PMMA with a measured hydroxyapatite density of 1000 $\pm 80\text{mg} \cdot \text{ml}^{-1}$. In total five 3 mm thick PMMA plates of 600 mm^3 where stacked in the milled hole, and the bone was placed in a water basin over the calibration phantom. A CT scan was made with the PMMA plates one by one replaced with HD-PMMA, thus simulating an increase in calcification. An overview of the in-vitro lesion model can be found in figure 6.

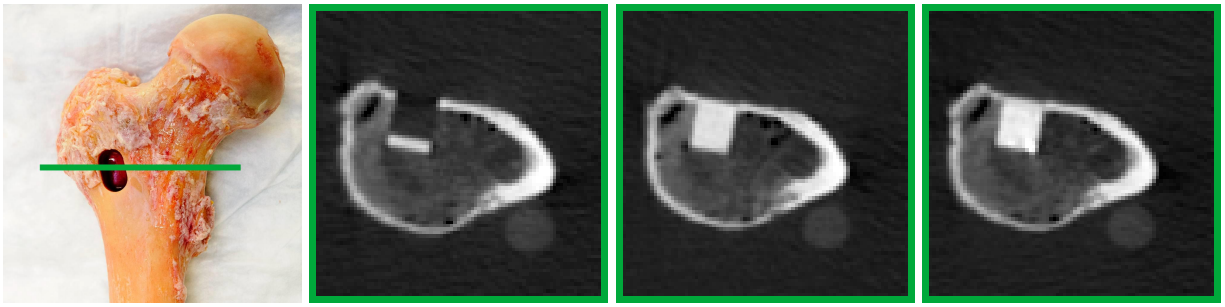

(a) In-vitro model (b) 1 × PMMA (c) 5 × PMMA (d) 5 × HD PMMA

Figure 6. Overview of the in-vitro lesion model. (a) Shows a photo of the milled hole in the intertrochantic region of the femur, with the line indication the location of the CT images in (b), (c) and (d). (b) Shows a single plate of PMMA in a water-filled hole. (c) Shows a intersection of the transversal CT slice with five PMMA plates, whereas (d) contains five HD-PMMA plates.

A ROI around the milled hole was manually segmented in the first scan, and transformed to the other scans in the series. In the intact contra-lateral femur a similar ROI was selected to be used as control. For the analysis, the mean calcification (figure 7) and empirical density distribution (figure 9) were used.

4. RESULTS

Using the validation phantom, the mean mineral density was calculated for a ROI containing the phantom lesion, approximately 21 cm^3. The ROI was transformed to the other volumes in the scans, in such a way that the increasing number of PMMA plates simulated an increasing calcification of a lesion site. This was done for both replacement of water with PMMA plates (referred to as the large changes study), and by the replacement of PMMA plates with HD pmma plates. The measured mean mineral density is shown in figure 7. The average prediction interval for these scans, taken from the calibration function, is ± 14.1 mg $\cdot$ ml^{-1}.

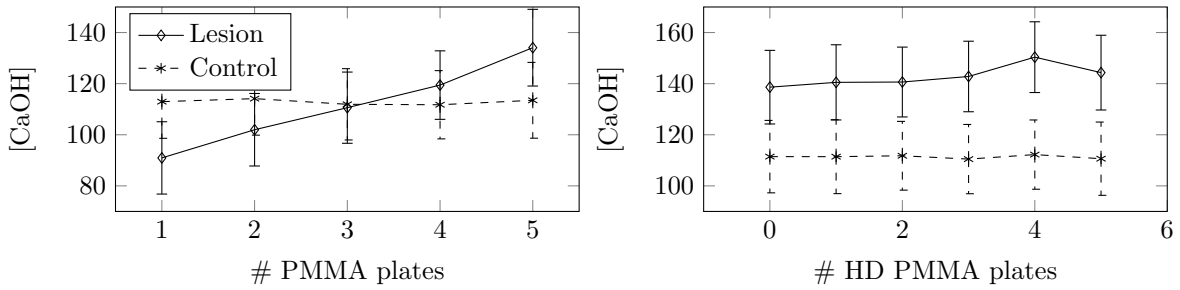

(a) Large changes study (b) Small changes study

Figure 7. Replacement study of the mean bone mineral density for the large changes (a) and the small changes(b) The black line depicts phantom lesion, while the dotted line indicates the mean value and prediction intervals of a similar ROI on the unaffected, contralateral side.

Another metric of interest was the density distribution, analyzed with the KS-test. For both the ROI around the lesion and the contralateral control ROI distributions were estimated. These can be found in figure 8 for the large changes, and figure 9 for the small changes.

The KS tests the null hypothesis that two empirical distributions share the same continuous distribution. These where cross-calculated for both studies. The results can be found in table 1 for the large changes, and in table

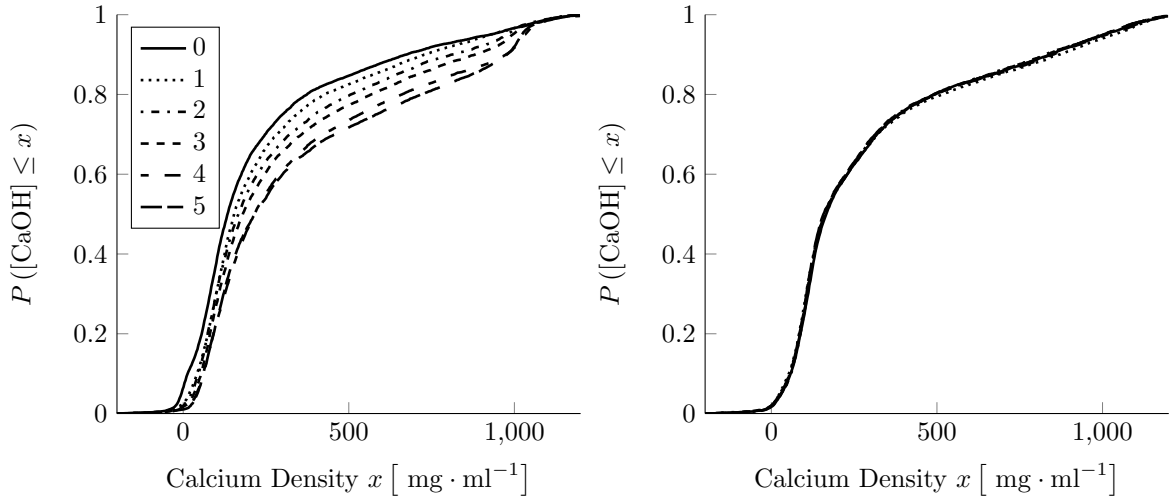

Figure 8. Large changes study empirical density distribution for the lesion model (a) and the control (b). The differences in calcium density distribution can clearly be seen in the phantom lesion, while the scans for the control have an equal distribution. The lines indicate the number of PMMA plates.

Table 1. Large changes study KS probabilities of the null hypothesis that emperical density distributions obtained from a registered ROI in the lesion model originate from the same continuous distribution. Bold values are rejections for $p \leq 0.05$.

Phantom Lesion

# PMMA	1	2	3	4	5
0	0.0529	**0.0000**	**0.0000**	**0.0000**	**0.0000**
1		**0.0026**	**0.0000**	**0.0000**	**0.0000**
2			**0.0140**	**0.0000**	**0.0000**
3				**0.0000**	**0.0000**
4					0.0953

Control

# PMMA	1	2	3	4	5
0	0.7075	0.7389	0.9995	0.9995	0.9999
1		0.3777	0.4882	0.9224	0.4882
2			0.6436	0.4591	0.7075
3				0.9020	0.9995
4					0.9224

2 for the small changes. Bold values indicate rejection of the null hypothesis. It can be seen that for the large changes study, a single plate change is detectable, while for the small changes study an increase of 3 plates is detectable in twothirds of the cases.

To get a qualitative opinion of the framework performance on real data, a small explorative study was performed. The framework was applied to the scans of a single patient with a large lytic (bone consuming) lesion in the proximal joint of one of the femurs. These scans were taken before, during, directly after and at follow up of This lesion is shown in figure 1 (c). The density distributions for a ROI containing the proximal side of the femur is shown in figure 10. In the first femur, which contained the lesion, a small deviation can be seen on the left side of the density distribution graph. This deviation is not visibly present in the second femur without lesion. However, the (omitted) KS test proved inconclusive on both femurs.

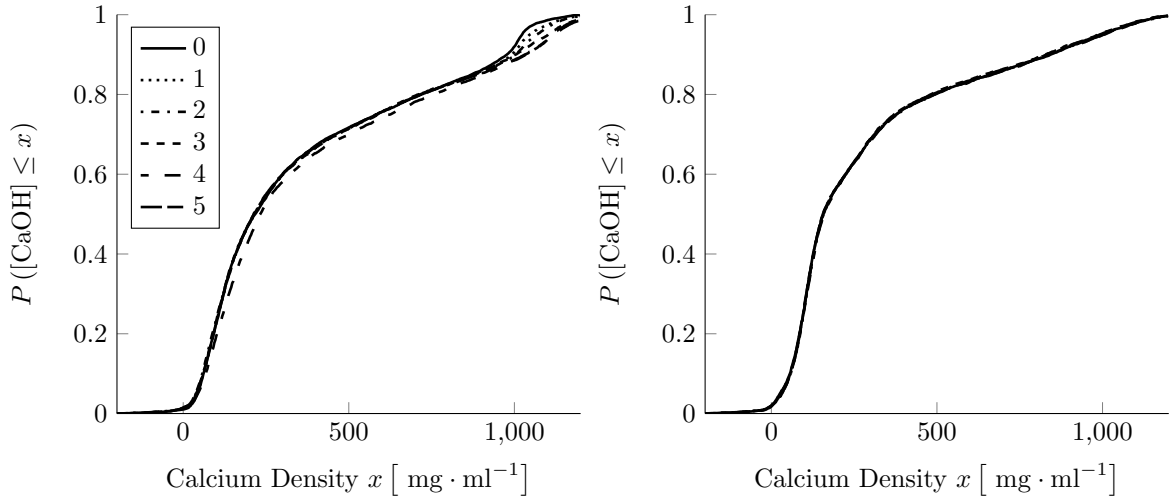

Figure 9. Replacement study emperical density distributions for the phantom lesion (a) and the control (b). The increase in calcium density from 888 to 1000 mg/ml can be seen in the (a) plot, while the scans for the control have an equal distribution. The lines indicate the number of HD-PMMA plates.

Table 2. Small changes in phantom lesion KS probabilities of the null hypothesis that two empirical density distributions obtained from a registered ROI of the in vitro model originate from the same continuous distribution. Bold values are rejections for $p \leq 0.05$. The controls are not shown, but were all accepted with $p \geq 0.5$.

Phantom lesion

#HD PMMA	1	2	3	4	5
0	0.4310	0.1494	**0.0026**	**0.0010**	**0.0003**
1		0.9680	0.1771	**0.0430**	**0.0348**
2			0.3287	0.1923	0.1370
3				0.3287	0.7992
4					0.5181

Control

# HD PMMA	1	2	3	4	5
0	0.9402	0.8276	0.7075	0.9995	0.8276
1		0.9911	0.8793	0.9402	0.8793
2			0.9856	0.7075	0.9973
3				0.5488	0.9973
4					0.7695

5. DISCUSSION

The results indicate that for small differences, simple one dimentional metrics often cannot discriminate changes in mineral density. This is likely caused by the relative large amount of noise present in the used CT scans. That way, the prediction interval rises, which makes such an analysis not very sensitive. This is illustrated by figure 7 (a), where only a difference of four PMMA plates with respect to water is detectable within statistical valid limits. Changes in real world lesions are probably much smaller.

The two-dimensional KS test however indicates that even on these coarse resolution CT scans small differences in mineralization can be detected, as indicated by figure 9. The small, localized difference in density distribution is a hard thing to prove. This is possible further complicated by the uncertainties introduces by the calibration process. An indication is the lowest line in figure 9(a), which is supossed to run evenly with the rest of the lines. A small error in the calibration offset can introduce differences that are not in correspondence with the actual situation.

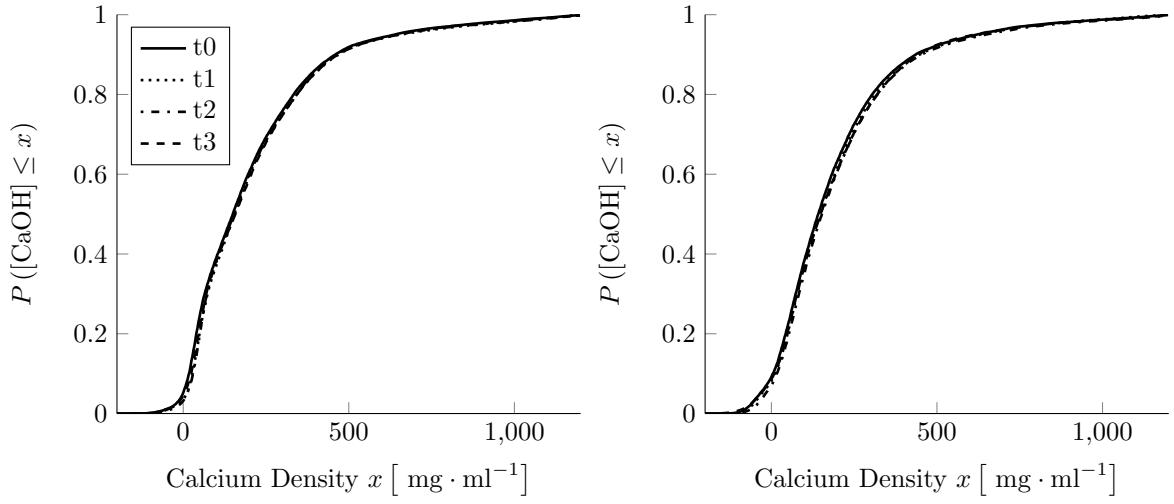

(a) Femur 1

(b) Femur 2

Figure 10. Empirical density distribution of the femoral head of patient 123. (a) Shows some small differences in calcification around the 50 $\mathrm{mg} \cdot \mathrm{ml}^{-1}$ point, probably due to the changes in the large lytic lesion present in this femur. Those differences are less visible in the femur without lesion, shown in (b).

6. CONCLUSION

In conclusion, the framework is able to statistically discriminate between small localized differences in mineralization of in-vitro phantom lesion model. In-vivo density changes that are not detectable to the naked eye can be made visible using the framework. Using a Kolmogorov-Smirnov test, changes in density distribution due to an increase of the calcium concentration could be discriminated. Changes in 8% of a 21 cm ROI around the artificial lesion 888 $\pm 57\mathrm{mg} \cdot \mathrm{ml}^{-1}$ to 1000 $\pm 80\mathrm{mg} \cdot \mathrm{ml}^{-1}$ could be statistically proven using the proposed framework. This makes it a promising tool in the analysis of the effects of different types of radiotherapy on metastatic lesions.

APPENDIX A. PROPERTIES OF BONE

Bone is the internal mechanical support which functions as main structure for motion, protector of vital organs, accomodation for blood producing cells and calcium reservoir.[15] The anatomy of bone can be split into multiple organization levels, as can be seen in figure 11. In this thesis, only organizational levels relevant for the imaging techniques used in this study will be addressed. These are mainly the two largest anatomical organisation levels.

A.1 Macroscopic anatomy of long bones

The macroscopic anatomy level is the largest organisation level, and consists of structures with a minimum size of about 0.1 mm. At this level, two different structures can be discerned,[17] The first structure is the diaphysis, or shaft, located at the center of the bone. It can be seen as a tube of cortical bone around a hollow inside containing the bone marrow. The inside is called the medullary cavity.

The second structure is located at both ends of the bone, the epiphyses are often a more bulbous structure. The outer layer consists of cortical bone, like in the diaphysis, only the inside is formed by cancellous (spongy) bone. In adults, the epiphysis is joined to the diaphysis by the epiphyseal line, the remainder of the growthplate (or ephyseal plate) in children.

A.2 Microscopic anatomy

As a next detail level after the gross anatomy, the microscopic level consists of the difference between cortical and cancellous bone. The level consists of structures with dimensions between 0.1 mm and 100 nm. Cortical

bone is the solid, dense material found on the outside of the bones. About 80% of the skeletal bone volume of an adult is cortical bone.[15] In long bones of adults like the *os femoris* it is structured in so-called Haversian systems (osteons), which are small tubular systems with stacked layers and a hollow core. Every layer has collagen fibers running parallel direction, while in the next layer the collagen runs in another direction. This way, rotational movements can be restrained.

Cancellous bone forms the other 20% of the skeletal mass of an adult human. It is a highly porous network of trabeculae of mainly lamellar bone. The bone volume fraction differs from 25% in the *os femoris* to 10% in some of the vertebrae.[15] According to a review article by Currey,[18] an important function of cancellous bone in the ephyphisis is to move the load on the joint to the more dense cortical bone. Therefore, the orientation of the trabeculae is in alignment with the direction of forces moving from the joint to the cortical bone. Also, the porous structure of cancellous bone means that it is lighter than cortical bone.

Smaller organizational levels of bone exist, but these are not distinguishable using conventional CT imaging. At the smallest organizational level, bone consists of collagen helices of about 300 nm length. The helices are connected at the long ends by mineral crystals of bone apatite, a form of hydroxyapatite with impurities as HPO_4, Na, Mg, citrate, carbonate, K and others.[16]

A.3 Bone strength

The strength of bones is a combination of tissue-level and structural properties of bone. It can not be defined by the mechanical properties of the elemental materials. At tissue-level, bone is somewhat of a composite material with anisotropic properties coming from the way the hydroxyapatite and collagen fibers are organized. At slightly larger structural level, the porosity shape of these trabeculae is of influence on the strength of bone. At even higher scale, cortical diameter and thickness have an effect as well. Besides that, the bone strength is not necessarily the sole predictor of fracture risk, since body mass, muscle force and physical activity have also influence on the load on the bone, and thus influence the chances that the bone will break.[19]

The strength of a bone can be changed by the body, through remodelling. Bone remodelling is an ongoing process in the body where old bone tissue is replaced by new.[19] This adapts the bone to changes in the quantity and direction of force. Besides, bone remodelling is a response to tissue damage as well. Damaged tissue, either due to overloading, radiotherapy or other factors, is replaced and strengthened. Although bone is a highly complicated an-isotropic material, the bone mass is a significant predictor of the strength of bone.[8]

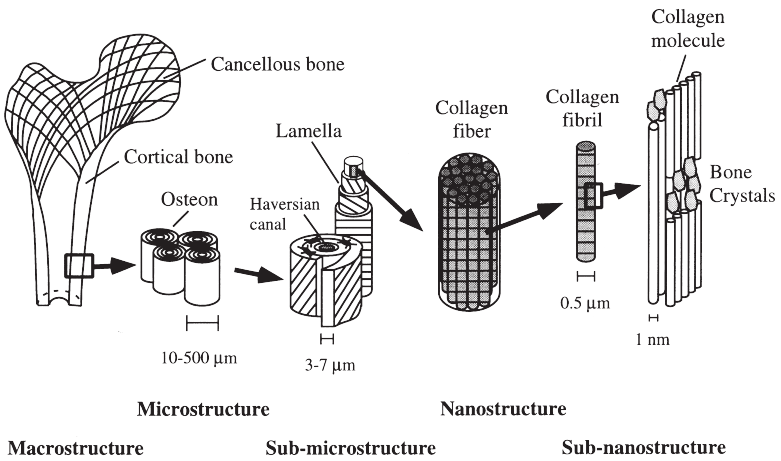

Figure 11. Different organizational levels of bone. In this introduction, only the macroscopic and microscopic anatomy are discussed. Source:.[16]

REFERENCES

[1] V. T. DeVita, T. S. Lawrence, and S. A. Rosenberg, *DeVita, Hellman, and Rosenberg's cancer: principles & practice of oncology. Vol. 2*, Wolters Kluwer/Lippincott Williams & Wilkins, 2008.

[2] J. Meeuse, Y. van der Linden, G. Van Tienhoven, *et al.*, "Efficacy of radiotherapy for painful bone metastases during the last 12 weeks of life: Results from the dutch bone metastasis study," *Cancer* **116**(11), pp. 2716–2725, 2010.

[3] Y. van der Linden, E. Steenland, W. Post, *et al.*, "Single-dose irradiation of painful bone metastases is as effective as multiple fractions. outcome of the dutch bone metastasis study," *Nederlands Tijdschrift voor Geneeskunde* **146**(35), pp. 1645–1650, 2002.

[4] E. Steenland, J. Leer, H. van Houwelingen, *et al.*, "The effect of a single fraction compared to multiple fractions on painful bone metastases: A global analysis of the dutch bone metastasis study," *Radiotherapy and Oncology* **52**(2), pp. 101–109, 1999.

[5] Y. M. van der Linden *et al.*, *Radiotherapy in bone metastases: the Dutch bone metastasis study.* PhD thesis, Leiden University, Leiden University Medical Center, Dept. of Clinical Oncology, 2005.

[6] S. Koswig and V. Budach, "Recalcification and pain relief following radiotherapy for bone metastases. a randomized trial of 2 different fractionation schedules (10 x 3 gy vs 1 x 8 gy)," *Strahlentherapie und Onkologie* **175**(10), pp. 500–508, 1999.

[7] H. Chen, B. Lee, H. Guo, *et al.*, "Changes in bone mineral density of lumbar spine after pelvic radiotherapy," *Radiotherapy and oncology* **62**(2), pp. 239–242, 2002.

[8] C. Hernandez, G. Beaupre, T. Keller, and D. Carter, "The influence of bone volume fraction and ash fraction on bone strength and modulus," *Bone* **29**(1), pp. 74–78, 2001.

[9] B. Arnold, "QCT-bone mineral phantom specsheet." personal comunication, 12 2013.

[10] N. Draper and H. Smith, *Applied Regression Analysis*, Wiley, New York, 1998.

[11] S. Klein, M. Staring, K. Murphy, M. A. Viergever, and J. Pluim, "Elastix: a toolbox for intensity-based medical image registration," *Medical Imaging, IEEE Transactions on* **29**(1), pp. 196–205, 2010.

[12] D. Shamonin, E. Bron, B. Lelieveldt, M. Smits, S. Klein, and M. Staring, "Fast parallel image registration on cpu and gpu for diagnostic classification of alzheimer's disease," *Frontiers in neuroinformatics* **7**, 2013.

[13] D. A. Darling, "The kolmogorov-smirnov, cramer-von mises tests," *The Annals of Mathematical Statistics* , pp. 823–838, 1957.

[14] M. Makita, K. Yamakado, A. Nakatsuka, *et al.*, "Effects of barium concentration on the radiopacity and biomechanics of bone cement: experimental study," *Radiation medicine* **26**(9), pp. 533–538, 2008.

[15] H. Koopman, F. de Jongh, and J. Homminga, *Biomechanics*, Coarse reader, Universiteit Twente, 11 2012.

[16] J. Rho, L. Kuhn-Spearing, and P. Zioupos, "Mechanical properties and the hierarchical structure of bone," *Medical Engineering and Physics* **20**(2), pp. 92–102, 1998.

[17] E. Marieb, *Human Anatomy & Physiology*, Pearson Benjamin Cummings, 6 ed., 2004.

[18] J. Currey, "The structure and mechanics of bone," *Journal of Materials Science* **47**(1), pp. 41–54, 2012.

[19] K. Davison, K. Siminoski, J. Adachi, *et al.*, "Bone strength: The whole is greater than the sum of its parts," *Seminars in Arthritis and Rheumatism* **36**(1), pp. 22–31, 2006.